THE JOURNAL OF BIOLOGICAL CHEMISTRY
Vol. 275, No. 2, Issue of January 14, pp. 1201–1208, 2000

Printed in U.S.A.

Structure-guided Transformation of Charybdotoxin Yields an Analog That Selectively Targets Ca^{2+}-activated over Voltage-gated K^+ Channels*

(Received for publication, October 7, 1999)

Heiko Rauer‡, Mark D. Lanigan§, Michael W. Pennington¶, Jayashree Aiyar‖, Sanjiv Ghanshani‡, Michael D. Cahalan‡, Raymond S. Norton§, and K. George Chandy‡**

From the ‡Department of Physiology and Biophysics, University of California, Irvine, California 92697, the §Biomolecular Research Institute, Parkville, 3052 Victoria, Australia, ¶Bachem Bioscience Incorporated, King of Prussia, Pennsylvania 19406, and the ‖Target Discovery Department, AstraZeneca Pharmaceuticals, Wilmington, Delaware 19850

We have used a structure-based design strategy to transform the polypeptide toxin charybdotoxin, which blocks several voltage-gated and Ca^{2+}-activated K^+ channels, into a selective inhibitor. As a model system, we chose two channels in T-lymphocytes, the voltage-gated channel *Kv1.3* and the Ca^{2+}-activated channel *IKCa1*. Homology models of both channels were generated based on the crystal structure of the bacterial channel *KcsA*. Initial docking of charybdotoxin was undertaken with both models, and the accuracy of these docking configurations was tested by mutant cycle analyses, establishing that charybdotoxin has a similar docking configuration in the external vestibules of *IKCa1* and *Kv1.3*. Comparison of the refined models revealed a unique cluster of negatively charged residues in the turret of *Kv1.3*, not present in *IKCa1*. To exploit this difference, three novel charybdotoxin analogs were designed by introducing negatively charged residues in place of charybdotoxin Lys^{32}, which lies in close proximity to this cluster. These analogs block *IKCa1* with ~20-fold higher affinity than *Kv1.3*. The other charybdotoxin-sensitive Kv channels, *Kv1.2* and *Kv1.6*, contain the negative cluster and are predictably insensitive to the charybdotoxin position 32 analogs, whereas the maxi-K_{Ca} channel, *hSlo*, lacking the cluster, is sensitive to the analogs. This provides strong evidence for topological similarity of the external vestibules of diverse K^+ channels and demonstrates the feasibility of using structure-based strategies to design selective inhibitors for mammalian K^+ channels. The availability of potent and selective inhibitors of *IKCa1* will help to elucidate the role of this channel in T-lymphocytes during the immune response as well as in erythrocytes and colonic epithelia.

Potassium channels are a diverse superfamily of ~80 integral membrane proteins that play crucial roles in many different physiological processes and are widely recognized as therapeutic targets. Venoms from spiders, scorpions, snakes, bees, and marine extracts have yielded polypeptide inhibitors of mammalian K^+ channels, many of which bind with high affinity to a vestibule at the external entrance of the channel pore. Some of these polypeptide toxins have been used as molecular calipers to estimate the dimensions of K^+ channel vestibules (1–7). Recently, the structure of the bacterial K^+ channel *KcsA* from *Streptomyces lividans* has been determined by x-ray crystallography (8). The turret region and the external pore of this channel correspond to the external toxin-binding vestibule in eukaryotic K^+ channels, and the crystallographic dimensions of the *KcsA* channel vestibule are remarkably similar to those estimated by toxin-mapping methods for eukaryotic K^+ channels (9). The convergence of these two approaches raises the possibility of exploiting structure-based strategies to design specific inhibitors that target pharmacologically relevant K^+ channel targets.

To test the feasibility of this approach, we have used charybdotoxin (ChTX),[1] a polypeptide that potently blocks the voltage-gated channel *Kv1.3* and the Ca^{2+}-activated channel *IKCa1*, both present in human T-lymphocytes (10, 11) to design an analog that selectively targets *IKCa1*. These two channels have been chosen as our model system since they are widely regarded as therapeutic targets. Both channels regulate the membrane potential of resting and activated T-cells and modulate the calcium signaling response that is essential for their activation (12). Inhibitors of these channels block the activation of human T-lymphocytes (13–15). Several potent and selective peptide and non-peptide inhibitors are available for *Kv1.3*. However, there is a dearth of selective blockers of the Ca^{2+}-activated *IKCa1* channel, and the most selective inhibitor of this channel, clotrimazole, also inhibits cytochrome P450-dependent enzymes (16–19). The *IKCa1* gene also encodes the "Gardos" channel in erythrocytes and is thought to encode the IK_{Ca} channel in colonic epithelial cells, platelets, and pancreatic islets (20–23). *IKCa1* inhibitors are currently being evaluated for prevention of chloride and water loss in diarrhea and for the treatment of erythrocyte dehydration in sickle cell disease (19, 24, 25). Highly specific blockers of the *IKCa1* channel may therefore have clinical use in both these ailments as well as a potential use as immunosuppressants.

In this study, we have constructed homology models of *IKCa1* and *Kv1.3* based on the crystal structure of the *KcsA* channel and performed preliminary docking of ChTX for heuristic purposes. The accuracy of these docking configurations

* This work was supported by National Institutes of Health Grants MH59222 (to K. G. C. and M. D. C.), NS14609 (to M. D. C.), and GM54221 (to M. W. P., R. S. N., and K. G. C.); by a gift from Merck Sharp and Dohme (to K. G. C.); and by a Feodor Lynen fellowship from the Alexander von Humboldt Foundation (to H. R.). The costs of publication of this article were defrayed in part by the payment of page charges. This article must therefore be hereby marked "*advertisement*" in accordance with 18 U.S.C. Section 1734 solely to indicate this fact.

** To whom correspondence should be addressed: Dept. of Physiology and Biophysics, Rm. 291, Joan Irvine Smith Hall, University of California Medical School, Irvine, CA 92697. Tel.: 949-824-2133; Fax: 949-824-3143; E-mail: gchandy@uci.edu.

[1] The abbreviations used are: ChTX, charybdotoxin; Fmoc, *N*-(9-fluorenyl)methoxycarbonyl; HPLC, high pressure liquid chromatography; Dap, diaminopropionic acid; Cpa, *p*-carboxyphenylalanine.

was tested by mutant cycle analysis that measures the strength of coupling between interactive pairs of toxin and channel residues (26). Using this approach, we have determined the ChTX docking configuration in both channels and identified a structural feature unique to the ChTX-*IKCa1* interaction surface. This paper describes the guided design and electrophysiological characterization of three novel ChTX analogs that specifically target this unique *IKCa1* motif.

MATERIALS AND METHODS

Reagents—Cell lines stably expressing mouse *Kv1.1*, rat *Kv1.2*, mouse *Kv1.3*, human *Kv1.4*, human *Kv1.5*, and mouse *Kv3.1* (27) were maintained in Dulbecco's modified Eagle's medium containing 10% fetal calf serum and G418 (1 mg/ml). The rat *Kv1.6* expression construct was a kind gift from Dr. O. Pongs (ZMNH, Hamburg, Germany). The human *IKCa1* expression construct (11) and the PCR-generated (28) *IKCa1*-Asn^{239} and *IKCa1*-Lys^{239} mutants (7) have been described. The *hSlo* (BK_{Ca}) expression construct was a kind gift from Dr. L. Toro (UCLA). Endogenously expressed IK_{Ca} and *Kv1.3* currents were studied in phytohemagglutinin-activated human T-lymphocytes, and endogenous SK_{Ca} currents were studied in the human Jurkat T-cell line (29, 30). Fetal calf serum, L-glutamine, penicillin, and streptomycin were obtained from Life Technologies, Inc.

Polypeptide Synthesis—Fmoc-derivatives were obtained from Bachem AG (Bubendorf, Switzerland). Solid-phase assembly was initiated with *t*-butyl-Fmoc-Ser resin. Automated stepwise assembly was carried out entirely on an ABI 431A peptide synthesizer (Applied Biosystems, Foster City, CA). The ChTX position 32 analogs were solubilized, oxidized, and purified by reversed-phase HPLC, and fractions were pooled and lyophilized. The structure and purity of the peptides were confirmed by reversed-phase HPLC, amino acid analysis, and electrospray ionization mass spectrometry analysis. Samples were weighed and adjusted to account for peptide content prior to bioassay. The ChTX-Asp^{25} analog has been described (4). Recombinant ChTX-Gln^{31}, ChTX-Glu^{31}, and ChTX-Orn^{27} were kind gifts from Dr. C. Miller (Brandeis University).

Homology Models of Kv1.3 and IKCa1—Fig. 1 shows the amino acid sequence of the turret region, pore, and parts of the inner helix of the *KcsA* channel aligned with the corresponding regions of *IKCa1* and *Kv1.3*. These channel regions interact with polypeptide toxin inhibitors, and mapping studies with these toxins have shown that the external vestibules of the *Kv1.3* and *IKCa1* channels are topologically similar to that of *KcsA* (7, 9, 31). Based on this alignment (>50% sequence identity) and published structural data for the *KcsA* channel (8), homology models of the *IKCa1* and *Kv1.3* vestibules were constructed and energy-minimized. Coordinates for *KcsA* (Protein Data Bank code 1BL8) were kindly supplied by Dr. MacKinnon (Rockefeller University). Residues in each subunit that were not defined in the crystal structure (Arg^{27}, Ile^{60}, Arg^{64}, Glu^{71}, and Arg^{117}) were inserted using the Biopolymer module of Insight98 (Molecular Simulations Inc., San Diego, CA). Models of *Kv1.3* and *IKCa1* were generated from the corrected structure by mutating appropriate *KcsA* residues (between positions 23 and 119) in Biopolymer, thus simulating the S5-P-S6 regions of the two larger mammalian channels (see Fig. 1). These models were energy-minimized in the CVFF force field of the Discover module of Insight98. 10,000 iterations were performed using the conjugate gradient algorithm with a 25-Å cutoff for non-bonded atoms and a distance-dependent dielectric in place of explicit water molecules (10,000 iterations were sufficient to bring each model to steady state).

K^+ channels possess a conserved selectivity filter, Gly-Tyr-Gly-Asp, located in the channel pore. In *KcsA*, the backbone carbonyl groups of this selectivity filter are arranged in the pore lumen so as to form a series of oxygen rings, the dimensions of which allow the coordination of desolvated K^+ ions. The Tyr side chains are oriented away from the pore and form hydrogen bonds with surrounding Trp side chains, suggesting the possibility that this acts like a spring to hold the pore open to the appropriate dimensions (8). In *KcsA*, this hydrogen bonding is observed between Tyr^{78} and Trp^{68}. Although a Trp^{67}-Trp^{68} diad is conserved in *Kv1.3* and *Shaker*, only the equivalent of Trp^{67} is found in *IKCa1* (Trp^{242}). Assuming that the spring mechanism exists in *IKCa1* as it does in *KcsA*, it is presumably mediated by Tyr^{253}–Trp^{242} hydrogen bonding. In an attempt to preserve the overall architecture of each channel model while allowing any mutated residues to find their respective local energy minima, the C^α atoms of all channel residues were fixed in Cartesian space during the course of energy minimization (and during subsequent molecular dynamics simulations). Our *Kv1.3* model is similar to that described previously (31), although the earlier model was constructed without access to the *KcsA* coordinates.

Docking of IKCa1 and Kv1.3 with ChTX—Energy-minimized channel models were juxtaposed with the closest-to-average conformation of ChTX in such a way as to preclude steric contact (typically this resulted in the closest possible contacts between ligand and receptor being ≥10 Å). ChTX was then positioned manually so that Lys^{27} was facing the pore and Arg^{25} was oriented toward channel residues, consistent with earlier studies (4). Further mutant cycle analyses were performed to test the ChTX-*IKCa1* interactions predicted by the docking model. To preserve the overall architecture of ChTX and the channel models during docking, various constraints were placed on both molecules prior to performing molecular dynamics. The C^α atoms of all channel residues were fixed in Cartesian space, and distances measured from the structure of ChTX (33 $d_{\alpha\alpha}(i,i+4)$ distances along the backbone of ChTX and 3 $d_{\alpha\alpha}$ distances, representing the disulfide bonds at positions 7–28, 13–33, and 17–35 were applied as constraints in Discover with a tolerance of ±0.1 Å and a force constant of 1000 kcal·mol^{-1}. Docking simulations were performed by first energy-minimizing the restrained ligand-receptor complex as outlined above, followed by 250 ps of molecular dynamics at 300 K with a 1.0-fs time step, a 25-Å cutoff for non-bonded atoms, and a distance-dependent dielectric. A 25-Å cutoff distance was used even though it lengthens the computation time because initial docking simulations with cutoff distances of 15 and 20 Å did not reproduce some expected interactions between charged side chains of the toxin and channel. After allowing ~50 ps for equilibration, the lowest van der Waals energy conformation was further energy-minimized as described above. Models of ChTX docked to *Kv1.3* and *IKCa1* were analyzed using Insight98. An alternative docking simulation was tried in which the turret region of the *Kv1.3* model (residues 373–379 of each subunit) was left unrestrained to determine what effect this might have on potential electrostatic interactions between it and the Lys^{32} region of ChTX. In this simulation, the turret moved outward (further away from ChTX) relative to the simulation in which it was restrained.

Electrophysiological Analysis—Each K^+ channel expression construct was specifically linearized and transcribed *in vitro*. As described earlier, the cRNA, together with a fluorescent fluorescein isothiocyanate dye, was injected into rat basophilic leukemia cells. Fluorescent cells were visualized after 2–6 h of incubation, and specific currents were measured using the patch-clamp technique (32, 33). Cells measured in the whole-cell configuration were bathed in mammalian Ringer's solution containing 160 mM NaCl, 4.5 mM KCl, 2 mM $CaCl_2$, 1 mM $MgCl_2$, and 10 mM HEPES (adjusted to pH 7.4 with NaOH) with an osmolarity of 290–320 mosM. The internal pipette solution for Kv recordings contained 134 mM potassium fluoride, 1 mM $CaCl_2$, 2 mM $MgCl_2$, 10 mM HEPES, and 10 mM EGTA (adjusted to pH 7.2 with KOH) with an osmolarity of 290–310 mosM, and these currents were measured following 200-ms depolarizing pulses to 40 mV from the holding potential every 30 s. The internal pipette solution for IK_{Ca} and SK_{Ca} recordings contained 135 mM potassium aspartate, 2 mM $MgCl_2$, 10 mM HEPES, 10 mM EGTA, and 8.7 mM $CaCl_2$ (adjusted to pH 7.2 with KOH) with an osmolarity of 290–310 mosM (free $[Ca^{2+}]_i = 10^{-6}$ M). Kv currents were activated by a 200-ms voltage step from a holding potential of −80 to 40 mV every 30 s. K_{Ca} currents were activated with 1 μM free $Ca^{2+}{}_i$ and 200-ms voltage ramps from −150 to 50 mV applied every 5 s (holding potential = −80 mV). For *hSlo* expression, 25–50 ng of cRNA was injected into *Xenopus laevis* oocytes 3 to 6 days prior to recording. The outside-out patch-clamp configuration was used to record macroscopic *hSlo* currents. For these experiments, the external solution contained 140 mM $NaMeSO_3$, 10 mM HEPES, 2 mM $MgCl_2$, and 2 mM KCl (adjusted to pH 7.4 with NaOH), whereas the internal solution contained 140 mM $KMeSO_3$, 10 mM HEPES, 2 mM $MgCl_2$, 2 mM KCl, and 1 mM H-EDTA, and $CaCl_2$ was added to obtain a free $[Ca^{2+}]_i$ of 5×10^{-5} M (adjusted to pH 7.2 with KOH). *hSlo* currents were activated with 50 μM free $Ca^{2+}{}_i$ and 200-ms voltage ramps from −80 to 80 mV applied every 5 s. Series-resistance compensation (80%) was used if the current exceeded 2 nA. Leak currents were subtracted using the P/8 procedure for Kv currents. K_d values were calculated using the equation $K_d = ([\text{toxin}]/((1/y) - 1))$ (y = unblocked fraction of current) and are shown as mean ± S.D. ($n \geq 4$).

Double-mutant Cycle Analysis—Toxin-channel interactions, predicted from the docking configuration of ChTX in *IKCa1*, were tested experimentally by mutant cycle analysis. This method evaluates the strength of the interaction between any given pair of channel and toxin residues. For each mutant cycle, we measured the potency (K_d) of ChTX and its analogs on *IKCa1* and its mutants. The change in coupling energy ($\Delta\Delta G$) for a given pair of ChTX-*IKCa1* residues and their mu-

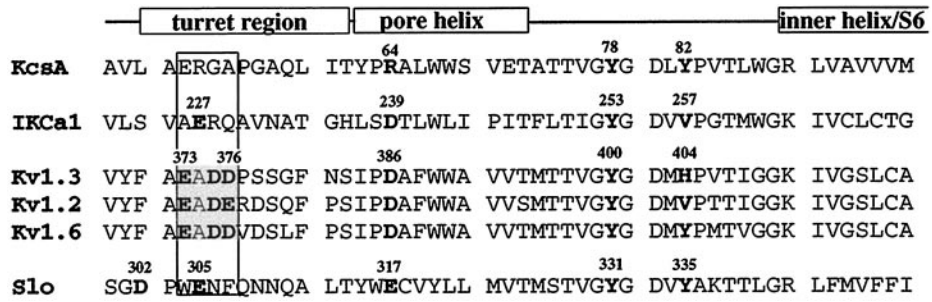

FIG. 1. **Amino acid sequence alignment of *KcsA*, *IKCa1*, *Kv1.3*, *Kv1.2*, *Kv1.6*, and *hSlo* showing sequence similarities >50%.** The positions of the turret region, pore, and inner helix are indicated, and critical amino acids are shown in *boldface*. The negatively charged cluster present in Kv channels (*shaded*), and homologous residues in K_{Ca} channels are *boxed*.

tants was calculated using the formula $\Delta\Delta G = kTln\Omega$, as described (7). Based on earlier studies (3, 26), $\Delta\Delta G$ values $\geq$0.5 kcal·mol^{-1} indicate that a pair of toxin and channel residues are likely to lie within 5 Å of each other.

RESULTS AND DISCUSSION

Overall Strategy

Our approach to design a selective inhibitor relies on the identification of a unique feature in the ChTX-*IKCa1* interface that is absent from the ChTX-*Kv1.3* binding surface. Therefore, the success of our comparative structure-based design strategy depends on understanding how ChTX interacts with the *IKCa1* and *Kv1.3* vestibules. To accomplish this, we developed homology models of the *Kv1.3* and *IKCa1* pore and vestibule regions (S5-P-S6 segments) based on the amino acid sequence alignment shown in Fig. 1 and the crystal structure of *KcsA* (see "Materials and Methods"). Initial docking of ChTX was performed based on published data for *Kv1.3* and then carried out for *IKCa1* under the assumption that ChTX may interact in a similar way. Both docking models were then tested by mutant cycle analyses, and these results were used to generate final refined docking models (Fig. 2). Comparison of the two docking models revealed a unique motif in the ChTX-*Kv1.3* interface that is absent in the ChTX-*IKCa1* binding surface, and three related ChTX analogs were designed to target this difference.

Docking of ChTX in Kv1.3

Several well characterized ChTX-*Kv1.3* interactions, previously identified by mutant cycle analyses and electrostatic compliance experiments (4), were used to dock ChTX in the vestibule of the *Kv1.3* model. In this configuration, Lys^{27} of ChTX protrudes into the pore in close proximity to *Kv1.3*-Tyr^{400} located in the selectivity filter. ChTX-Arg^{25} interacts with *Kv1.3*-Asp^{386} (in one subunit) and *Kv1.3*-His^{404} (from two adjacent subunits). The docking model based on these data also predicts an interaction between ChTX-Lys^{31} and *Kv1.3*-Asp^{386} in the subunit diametrically opposite to that interacting with ChTX-Arg^{25}. Mutant cycles were therefore performed with ChTX(Lys^{31} $\rightarrow$ Glu)-*Kv1.3*(Asp^{386} $\rightarrow$ Lys) and ChTX(Lys^{31} $\rightarrow$ Gln)-*Kv1.3*(Asp^{386} $\rightarrow$ Lys); these yielded $\Delta\Delta G$ values of 1.35 and 0.74 kcal·mol^{-1}, respectively, indicating that *Kv1.3*-Asp^{386} and ChTX-Lys^{31} lie within 5 Å of each other (26). Consistent with our results, Lys^{31} in agitoxin has been reported to couple to the residue in the *Shaker* channel (Asp^{431}) that is homologous to *Kv1.3*-Asp^{386} (3, 6).

Docking ChTX in IKCa1 Based on Its Docking with Kv1.3

The polypeptide toxin ChTX blocks *Kv1.3* (K_d = 2 nM) and *IKCa1* (K_d = 5 nM) with almost identical potency (10, 11, 30), and another toxin, *Stichodactyla helianthus* toxin, utilizes a similar core-binding domain to bind to both channels (7), albeit with very different potencies (16 pM *versus* 30 nM). Hence, ChTX might be expected to sit in the *IKCa1* vestibule with a similar geometry to that in *Kv1.3*. Guided by the ChTX-*Kv1.3* docking model, a docking simulation of ChTX in the *IKCa1* vestibule was performed for heuristic reasons. This docking model predicts that *IKCa1*-Asp^{239}, the residue homologous to *Kv1.3*-Asp^{386} (Fig. 1), lies in close proximity to ChTX-Arg^{25} and ChTX-Lys^{31}, but not to ChTX-Lys^{32}. In this model, the critical ChTX residue, Lys^{27}, protrudes into the channel pore and lies in the vicinity of Tyr^{253} in the selectivity filter. These docking models were tested experimentally by evaluating the coupling energy of specific residues predicted to be in close proximity and then refined. Specifically, we determined the coupling energies for the following pairs of specific toxin/channel residues using mutant cycle analyses: ChTX-Arg^{25}/*IKCa1*-Asp^{239}, ChTX-Lys^{31}/*IKCa1*-Asp^{239}, ChTX-Lys^{32}/*IKCa1*-Asp^{239}, and ChTX-Lys^{27}/*IKCa1*-pore.

Mutant Cycle Analyses of Predicted Docking Configuration

ChTX-Arg^{25} and ChTX-Lys^{31} Interactions with IKCa1-Asp^{239}—Replacement of the negatively charged residue Asp^{239} in *IKCa1* with the neutral asparagine (Asn^{239}) reduced the K_d for native ChTX by ~14-fold. A more substantial reduction in affinity of ~180-fold was observed when a positively charged lysine (*IKCa1*-Lys^{239}) was introduced at this channel position (Fig. 3, *A* and *B*). Neither mutation altered the biophysical properties of the channel. Charge reversal mutations at ChTX positions 25 (Arg^{25} $\rightarrow$ Asp) and 31 (Lys^{31} $\rightarrow$ Glu) also dramatically decreased toxin affinity by ~1325- and ~47-fold, respectively, for the wild-type *IKCa1* channel (Fig. 3, *A–C*). In contrast, a similar mutation at ChTX position 32 (Lys^{32} $\rightarrow$ Asp) decreased affinity by only 9-fold (Fig. 3*D*).

Thermodynamic double-mutant cycle analyses were performed to measure the change in coupling energy between *IKCa1*-Asp^{239} and each of the three ChTX residues Arg^{25}, Lys^{31}, and Lys^{32}. The $\Delta\Delta G$ values for the mutant cycles shown in Fig. 3*B* are 2.25 and 3.1 kcal·mol^{-1}, respectively, indicating that *IKCa1*-Asp^{239} and ChTX-Arg^{25} lie within 5 Å of each other. Strong coupling was also seen between *IKCa1*-Asp^{239} and ChTX-Lys^{31}, with the coupling energies being 1.9 and 2.4 kcal·mol^{-1} for the two cycles shown in Fig. 3*C*. In contrast, the $\Delta\Delta G$ of 0.02 kcal·mol^{-1} for the cycle in Fig. 3*D* indicates that *IKCa1*-Asp^{239} and ChTX-Lys^{32} are not energetically coupled.

ChTX-Lys^{27} Interactions with the Pore of IKCa1—Two approaches were used to test the proximity of ChTX-Lys^{27} to the *IKCa1* pore, the first showing that it lies close to a K^+-binding site and the second demonstrating that a shorter analog at this position (ChTX-Orn^{27}) interacts with a residue at the outer mouth of the pore.

All K^+ channel toxin inhibitors contain a critical lysine residue (in this case, ChTX-Lys^{27}) that projects into the channel pore (34) and lies close to a K^+-binding site near the conserved tyrosine (Tyr^{400} in *Kv1.3*) in the selectivity filter (5–7, 9, 31). Occupancy of this site by K^+ ions destabilizes toxin interactions with *Kv1.3* via electrostatic repulsion of this critical lysine (5–7). If ChTX-Lys^{27} lies close to a K^+-binding site near Tyr^{253} in the selectivity filter of the *IKCa1* pore, then occupancy of this site by K^+ ions should reduce the affinity of the

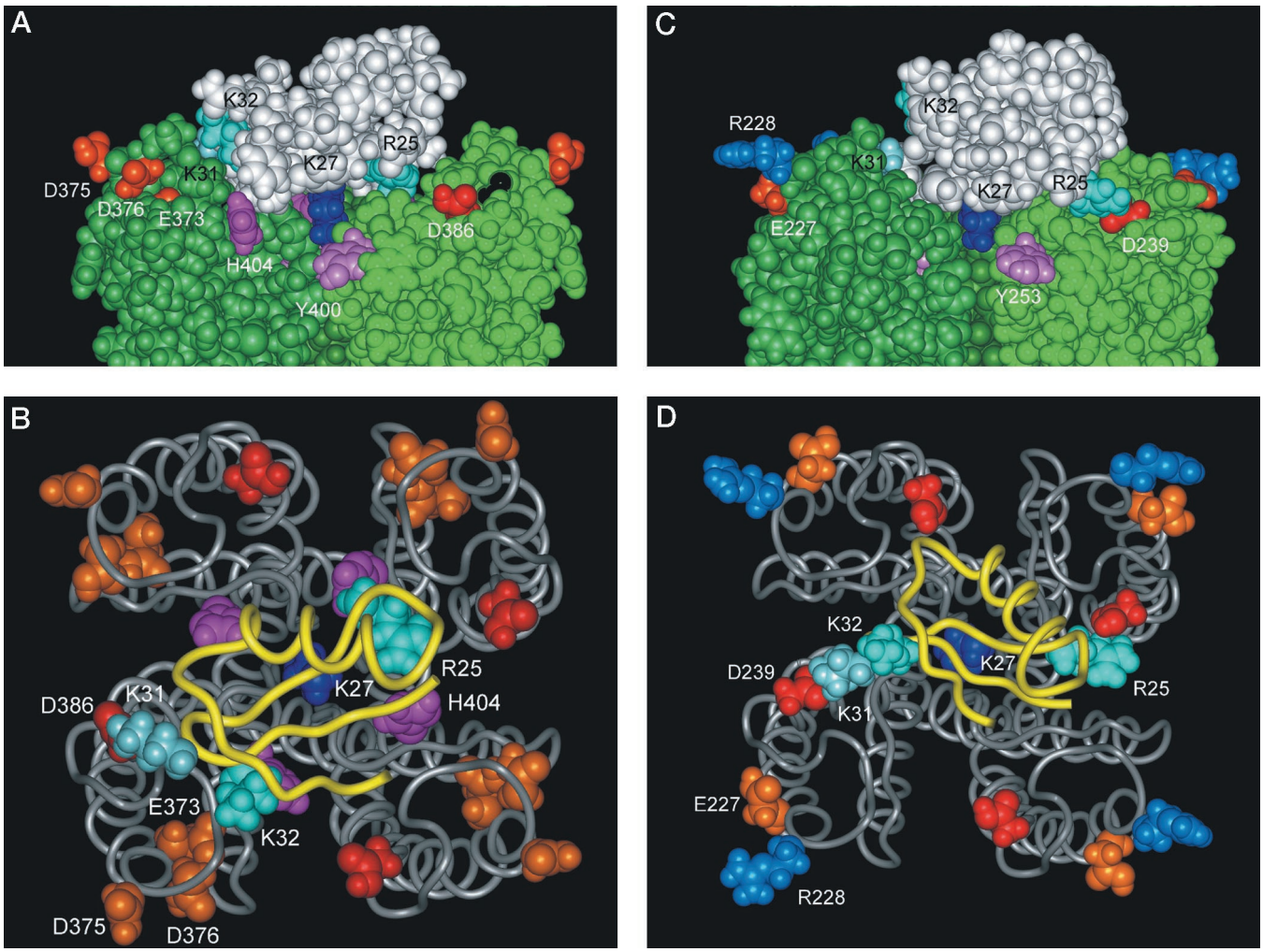

FIG. 2. **Homology models of the *Kv1.3* and *IKCa1* pore regions based on the *KcsA* structure.** *A*, side view of ChTX docked in the external vestibule of *Kv1.3*. The channel subunit nearest the viewer has been removed for clarity, and the remaining channel subunits are shaded in different *greens*. Other side chains are colored as follows: ChTX-Arg^{25} and ChTX-Lys^{32}, *cyan*; ChTX-Lys^{27}, *dark blue*; ChTX-Lys^{31}, *sky blue*; *Kv1.3*-His^{404}, *magenta*; *Kv1.3*-Tyr^{400}, *purple*; *Kv1.3*-Asp^{386}, *red*; and *Kv1.3*-Glu^{373}, *Kv1.3*-Asp^{375}, and *Kv1.3*-Asp^{376}, *orange*. *B*, top view of *Kv1.3* docked with ChTX. The backbone is shown as *ribbons*, and selected side chains are shown as Corey-Pauling-Koltun surfaces. *C*, side view of ChTX docked in the external vestibule of *IKCa1*. Colors are as the same as described for *A*, except as follows: Tyr^{253}, *purple*; Arg^{228}, *blue*; Glu^{227}, *orange*, and Asp^{239}, *red*. *D*, top view of *IKCa1* docked with ChTX as shown for *B*.

toxin for the channel. We tested this by examining the effect of increasing the external K^+ concentration from 4.5 to 164 mM on the affinity of the *IKCa1* channel for ChTX-Lys^{27}. As a control, we also performed this experiment using the ChTX analog ChTX-Dap^{27}, in which Lys^{27} was replaced by the shorter (2.5 Å) positively charged non-natural amino acid diaminopropionic acid. Earlier studies on *Kv1.3* have shown that Dap^{27} interacts with His^{404} at the entrance of the pore (5), rather than with the K^+-binding site in the selectivity filter, and the same may be true for *IKCa1*. Therefore, the interaction of Dap^{27} with the *IKCa1* pore should be insensitive to changes in the external K^+ concentration. Consistent with our prediction, the mutant cycle shown in Fig. 4*A* yields a strong coupling energy ($\Delta\Delta G$ = 0.76 kcal·mol^{-1}), indicating that ChTX-Lys^{27} lies within 5 Å of a K^+-binding site located in the *IKCa1* pore. Interestingly, the critical lysine at position 22 in the sea anemone *S. helianthus* toxin also interacts with a K^+-binding site within the pore of the *IKCa1* channel, and the affinity of *S. helianthus* toxin for *IKCa1* is reduced as the external K^+ concentration is increased (7).

We also examined the sensitivity of *Kv1.3* and *IKCa1* to the analog ChTX-Orn^{27}, in which the shorter positively charged ornithine (side chain length of 5.0 Å) was substituted for the critical Lys^{27} residue (chain length of 6.3 Å). As shown in Fig. 4*B*, this analog blocked *Kv1.3* in the nanomolar range (K_d = 196 nM), but was significantly less effective against *IKCa1* (K_d = 3300 nM). Since ChTX-Lys^{27} protrudes into the pores of both *IKCa1* and *Kv1.3*, why does ChTX-Orn^{27} have lower affinity for *IKCa1* than for *Kv1.3*? The outer pore regions of both channels are almost identical (Fig. 1), except for the presence of a histidine (His^{404}) at the entrance to the *Kv1.3* pore in place of valine (Val^{257}) in *IKCa1*. To determine whether this difference might contribute to the differential sensitivity to ChTX-Orn^{27}, we replaced *Kv1.3*-His^{404} with valine and measured the affinity of ChTX-Orn^{27} for this mutant channel, which more closely resembles the *IKCa1* pore. In keeping with our hypothesis, ChTX-Orn^{27} blocked *Kv1.3*-Val^{404} with an affinity similar to that for *IKCa1* and significantly less than that for wild-type *Kv1.3* (Fig. 4*B*). We were unable to determine the effect of the reverse mutation (Val^{257} → His) on the sensitivity of *IKCa1* to ChTX-Orn^{27} since this mutant channel is nonfunctional.

Refinement of the Docking Models

Our mutant cycle studies demonstrate that ChTX-Arg^{25} and ChTX-Lys^{31} interact with *IKCa1*-Asp^{239} in different subunits, whereas ChTX-Lys^{27} lies close to a K^+-binding site in the pore.

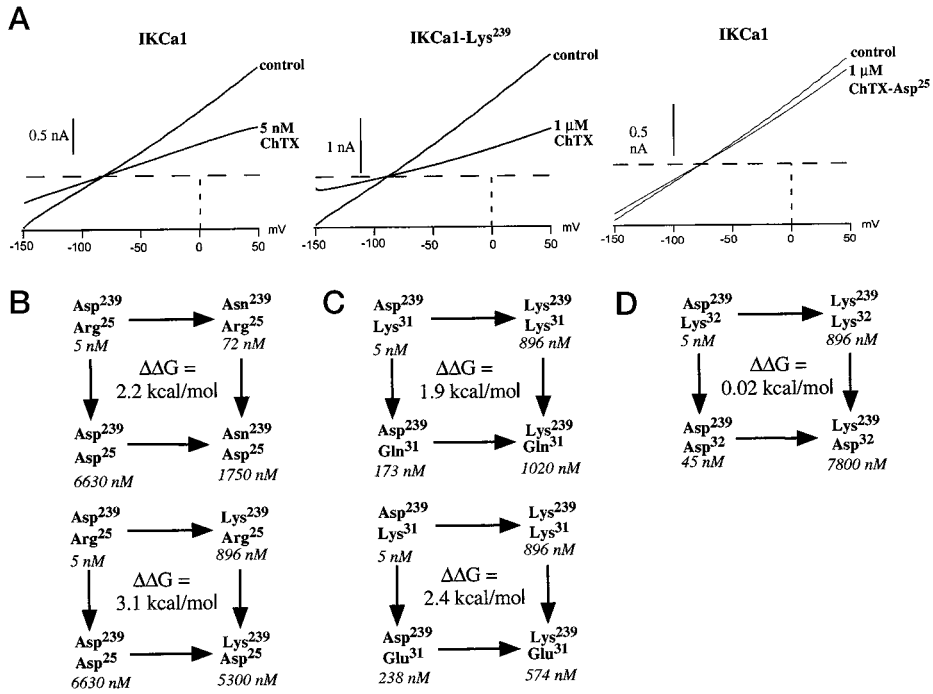

FIG. 3. **Interaction of the polypeptide toxin ChTX with the *IKCa1* channel.** *A*: *left panel*, representative *IKCa1* currents in the presence and absence of 5 nM ChTX (ChTX K_d = 5 ± 2 nM); *middle panel*, currents through the mutant channel *IKCa1*-Lys^{239} in the presence and absence of 1 μM ChTX (ChTX K_d = 896 ± 176 nM); *right panel*, *IKCa1* currents in the presence and absence of 1 μM mutant ChTX-Asp^{25} (ChTX-Asp^{25} K_d = 6630 ± 1350 nM). *B*: mutant cycles and coupling energies (ΔΔ*G*) of *IKCa1*-Asn^{239} and *IKCa1*-Lys^{239} with ChTX-Asp^{25}. *C*: mutant cycles and coupling energies of *IKCa1*-Lys^{239} with ChTX-Gln^{31} and ChTX-Glu^{31}. *D*: mutant cycle and coupling energy of *IKCa1*-Lys^{239} with ChTX-Lys^{32}.

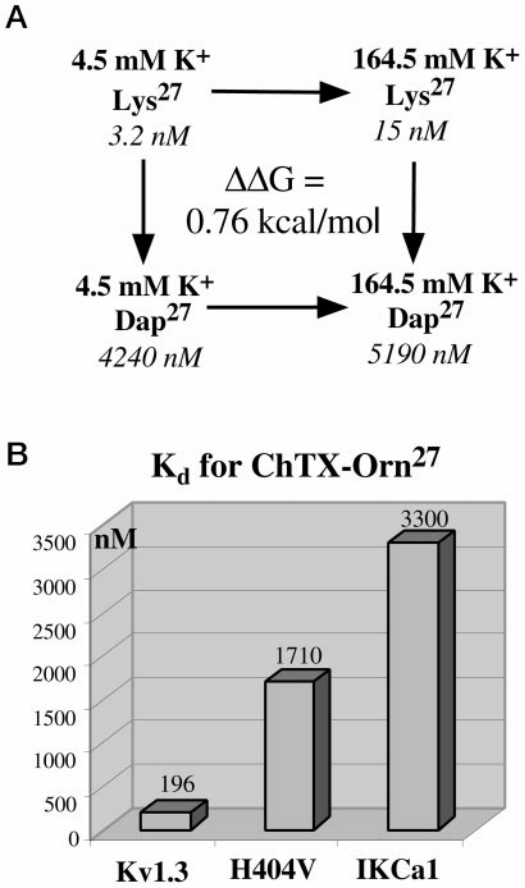

FIG. 4. **Interaction of ChTX-Lys^{27} with the pore of *IKCa1*.** *A*, mutant cycle with native ChTX and the analog ChTX-Dap^{27} on *IKCa1* in the presence of 4.5 and 164.5 mM external K^+. *B*, K_d values for the toxin analog ChTX-Orn^{27} on *Kv1.3* (K_d = 196 ± 27 nM), *Kv1.3*-Val^{404} (*H404V*) (K_d = 1710 ± 280 nM), and *IKCa1* (K_d = 3300 ± 813 nM).

The docking configuration of ChTX with both models was recalculated using these experimental data as restraints in molecular dynamics simulations (Fig. 2). Where significant coupling was observed between toxin and channel residues ($\Delta\Delta G > 0.7$ kcal·mol^{-1}), a target distance (as noted below) was applied between specific atoms from each residue with a 50 kcal·mol^{-1} force constant (31). Thus, docking constraints were applied between the following pairs of atoms: ChTX-*Kv1.3* docking, Lys^{27} N$^{\zeta}$ –Tyr^{400} C$^{\beta}$ (from all four subunits), Arg^{25} C$^{\zeta}$–His^{404} N$^{\delta 1}$ (from two adjacent subunits, target distance of 8.0 Å), and Lys^{31} N$^{\zeta}$–Asp^{386} C$^{\gamma}$ (from a single subunit, target distance of 6.0 Å); and ChTX-*IKCa1* docking, Lys^{27} N$^{\zeta}$–Tyr^{253} C$^{\beta}$ (from all four subunits), Arg^{25} C$^{\zeta}$–Asp^{239} C$^{\gamma}$ (from a single subunit), and Lys^{31} N$^{\zeta}$–Asp^{386} C$^{\gamma}$ (from a single subunit, target distance of 6.0 Å).

The final docking configurations of ChTX with *Kv1.3* and *IKCa1* (Fig. 2) place the toxin in similar orientations in the two channels, highlighting the usefulness of homology modeling approaches in defining toxin-channel interactions. In the case of *Kv1.3*, the orientation of the toxin about the pore axis is guided by the proximity of Arg^{25} to His^{404}. Coupling of Arg^{25} to two His^{404} side chains in adjacent subunits brings the former in closer proximity to Asp^{386}, an interaction alluded to by Aiyar *et al.* (5), than if Arg^{25} is coupled to only one His^{404} side chain. This docking configuration of ChTX with *Kv1.3* matches closely the ChTX docking configuration with *IKCa1* (Fig. 2). Thus, ChTX utilizes the same three key residues, Arg^{25}, Lys^{27}, and Lys^{31}, to interact with homologous residues in the external vestibules of *Kv1.3* and *IKCa1*. ChTX-Arg^{25} and ChTX-Lys^{31}, positioned at opposite ends of the toxin, interact with *Kv1.3*-Asp^{386} and *IKCa1*-Asp^{239} in diametrically opposite subunits of these channel tetramers. ChTX-Lys^{27}, located at the center of the channel-binding surface in the toxin, projects into the pores and lies close to the selectivity filter of both channels. A similar toxin-channel interaction has also been shown for *S. helianthus* toxin, which utilizes a conserved core domain to interact with *Kv1.3* and *IKCa1* (7) despite having a structural fold that bears no resemblance to ChTX (35).

Comparison of the Refined IKCa1 and Kv1.3 Models: Identification of a Unique Feature in IKCa1

The amino acid sequences and refined models of *IKCa1* and *Kv1.3* were compared to identify structural features unique to *IKCa1*. The sequence alignment in Fig. 1 shows a cluster of

three negatively charged residues, Glu^{373}, Asp^{375}, and Asp^{376}, in the turret region of *Kv1.3* (*shaded*) that are not present in *IKCa1*. The *Kv1.3* model (Fig. 2, *A* and *B*) shows the locations of these three acidic residues within the vestibule of *Kv1.3*. Glu^{373} and Asp^{376} are oriented toward the center of the channel pore, whereas Asp^{375} is at the outer edge of the turret. The docking configuration of ChTX in *Kv1.3* indicates that ChTX-Lys^{32} lies in the vicinity of Glu^{373} and Asp^{376}, although the terminal ammonium group of this Lys^{32} is ~10 Å away. No intermolecular constraints were applied among any of these residues during the docking, but if a weak constraint was included between Asp^{376} C^{γ} and Lys^{32} N, the distance from Lys^{32} to this part of the turret decreased to ~8 Å, without any significant change elsewhere. Based on this observation, the introduction of a negatively charged residue at ChTX position 32 might therefore significantly reduce the affinity of such an analog for *Kv1.3* via electrostatic repulsion.

IKCa1 contains two neutral residues (Ala^{226} and Gln^{229}) and one basic residue (Arg^{228}) (Figs. 1 and 2, *C* and *D*) in place of the acidic residues in the turret of *Kv1.3*. The only negatively charged residue in the turret region of *IKCa1* (Glu^{227}) is located at the outer edge of the turret, pointing away from the center of the vestibule (Fig. 2,*C* and *D*), and is therefore unlikely to interact directly with any ChTX residues. In contrast to *Kv1.3*, a ChTX analog containing a negatively charged residue at position 32 would be expected to retain most of its potency against the *IKCa1* channel.

Introduction of Negatively Charged Residues at Position 32 in ChTX Results in Analogs Selective for IKCa1 over Kv1.3

To test these predictions, we replaced Lys^{32} in ChTX with glutamate and tested the affinities of this novel analog (ChTX-Glu^{32}) and native ChTX for the cloned *IKCa1* and *Kv1.3* channels. Native ChTX blocked both *IKCa1* and *Kv1.3* in the low nanomolar range with K_d values of 5 and 2 nM, respectively (Figs. 5, *A* and *B*, and 6). As anticipated from our model, introduction of a negatively charged residue at ChTX position 32 reduced the affinity of this analog for *Kv1.3* by ~350-fold while only minimally affecting (~6-fold) its affinity for *IKCa1*. Thus, ChTX-Glu^{32} exhibits a ~20-fold higher affinity for *IKCa1* than for *Kv1.3*.

Since both channels are expressed endogenously in activated human T-lymphocytes, we also examined the effect of the ChTX-Glu^{32} analog on native *IKCa1* and *Kv1.3* currents. Fig. 5*C* shows a ramp protocol eliciting K^+ currents in activated human T-lymphocytes. *IKCa1* was the main carrier of K^+ currents at potentials more negative than −40 mV, whereas at depolarized potentials, K^+ currents were carried by a combination of *IKCa1* and *Kv1.3* channels. Consistent with the results on the cloned channels, the voltage-dependent *Kv1.3* current in activated T-lymphocytes was affected only minimally by 250 nM ChTX-Glu^{32} (Fig. 5*C*), a concentration that blocked ~25% of the cloned *Kv1.3* current, whereas this concentration of ChTX-Glu^{32} almost completely inhibited *IKCa1* currents. In contrast, native ChTX blocked both channels equally in the low nanomolar range (Fig. 5*C*). These results show that ChTX-Glu^{32} is a selective and potent inhibitor of the cloned *IKCa1* channel and its native counterpart in human T-lymphocytes compared with *Kv1.3*.

Encouraged by the selective properties of ChTX-Glu^{32}, we generated two additional ChTX analogs. The negatively charged residues aspartate (ChTX-Asp^{32}) and *p*-carboxyphenylalanine (ChTX-Cpa^{32}) were substituted for Lys^{32} in ChTX to investigate the influence of the side chain length on potency and selectivity. The aspartate side chain is shorter (3.1 Å) than

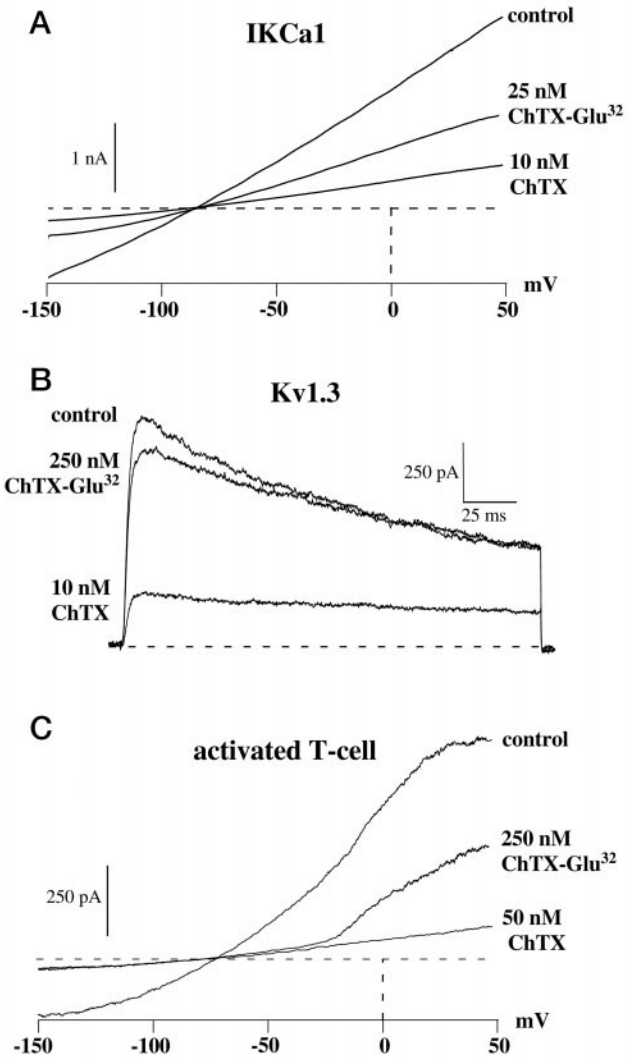

FIG. 5. **Specifically designed novel analog ChTX-Glu^{32} blocks *IKCa1* currents with an ~20-fold higher affinity than *Kv1.3* currents.** *A*, *IKCa1* currents in the absence and presence of native ChTX (K_d = 5 ± 2 nM) and ChTX-Glu^{32} (K_d = 33 ± 8 nM). *B*, *Kv1.3* currents in the absence and presence of ChTX (K_d = 2 ± 1 nM) and ChTX-Glu^{32} (K_d = 693 ± 117 nM). *C*, block of endogenous *IKCa1* and *Kv1.3* currents in human T-lymphocytes, activated for 72 h with phytohemagglutinin, by native ChTX and ChTX-Glu^{32}.

in glutamate (4.6 Å), whereas the *p*-carboxyphenylalanine side chain is longer (7.3 Å). ChTX-Asp^{32} and ChTX-Cpa^{32} blocked *IKCa1* channels significantly more potently than *Kv1.3* (Fig. 6), although ChTX-Glu^{32}, the analog with the intermediate-sized side chain, was the most selective because it exhibited the greatest difference in affinity between *IKCa1* and *Kv1.3*. Thus, using a structure-based homology modeling strategy, we predicted a novel toxin-channel interaction that was exploited in the design and engineering of three novel ChTX analogs (ChTX-Asp^{32}, ChTX-Glu^{32}, and ChTX-Cpa^{32}). Each of them contains a negatively charged residue at position 32 and selectively blocks *IKCa1* channels while being significantly less effective against *Kv1.3*.

Selectivity Profile of the ChTX Position 32 Analogs

ChTX is reported to block three other K^+ channels potently besides *IKCa1* and *Kv1.3*, including the voltage-gated K^+ channels *Kv1.2* (27) and *Kv1.6* (36) and the large-conductance Ca^{2+}-activated K^+ channel *hSlo* (37, 38). In an attempt to predict the behavior of the ChTX position 32 analogs on these channels, we

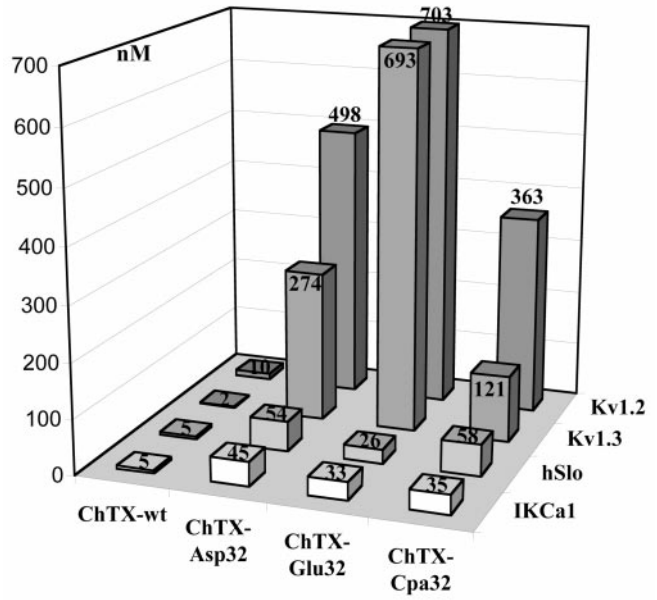

FIG. 6. **Selectivity profile of the novel ChTX position 32 analogs on all ChTX-sensitive K^+ channels.** Shown is a K_d value comparison of native ChTX (*ChTX-wt*) and the ChTX position 32 analogs ChTX-Asp[32] (side chain length of 3.1 Å), ChTX-Glu[32] (4.6 Å), and ChTX-Cpa[32] (7.3 Å) on the K_{Ca} channels *IKCa1* and *hSlo* and the Kv channels *Kv1.3* and *Kv1.2*. ChTX-Glu[32] was most potent and selective for *IKCa1* and *hSlo*. ChTX-Asp[32] and ChTX-Cpa[32] were less selective than ChTX-Glu[32]. *Kv1.3* and *Kv1.2* were weakly blocked with a similar profile by all three analogs.

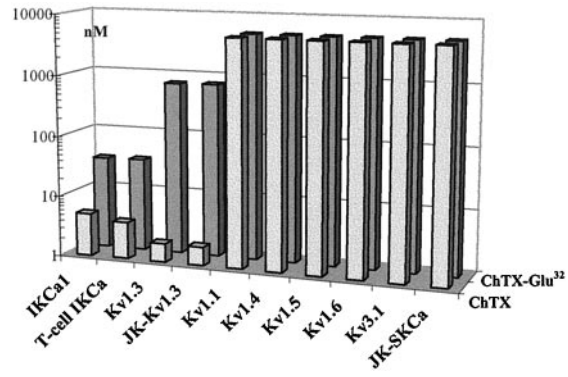

FIG. 7. **Selectivity profile of ChTX and ChTX-Glu[32].** Shown are the K_d values for *Kv1.1*, *Kv1.4*, *Kv1.5*, *Kv1.6*, and *Kv3.1* as well as the SK_{Ca} channel endogenously present in human Jurkat T-cells (*JK-SKCa*) with native ChTX and ChTX-Glu[32]. The K_d values for the cloned *Kv1.3* and *IKCa1* channels and for the endogenous *IKCa1* (native T-cells) and *Kv1.3* (Jurkat T-cells; *JK-Kv1.3*) channels are shown for comparison.

compared the amino acid sequences of the turret regions of these channels with those of *Kv1.3* and *IKCa1*. *Kv1.2* and *Kv1.6* channels both contain a negatively charged cluster at the position homologous to that in *Kv1.3* (Fig. 1). If the vestibules of these channels have a similar architecture to that of *Kv1.3*, they would exhibit a lower affinity for the ChTX position 32 analogs compared with wild-type ChTX. In contrast, *hSlo* has only two negatively charged residues in the turret region, Glu^{305} and Asp^{302} (Fig. 1). If its vestibule has a comparable topology to that of *IKCa1*, *hSlo*-Glu^{305} and *hSlo*-Asp^{302} would be at the same positions as *IKCa1*-Glu^{227} and *IKCa1*-Ser^{224}, respectively (Fig. 2,*C* and *D*), and neither residue would lie in close proximity to ChTX-Lys^{32}. Therefore, the introduction of negatively charged residues at this toxin position should have little effect on toxin potency for *hSlo*. In keeping with our predictions, the introduction of negatively charged residues at position 32 in ChTX significantly reduced the affinity of the three analogs for *Kv1.2* in a similar fashion to *Kv1.3* while only minimally affecting their affinity for *hSlo*. We found that the *Kv1.6* channel was insensitive to ChTX, in contradiction to some published data (36), but in confirmation of other studies (39). Consequently, *Kv1.6* was also resistant to the ChTX-Glu^{32} analog (Fig. 7). Since our comparative modeling approach accurately predicted the sensitivity of the *Kv1.2* and *hSlo* channels to the three ChTX position 32 analogs, it is likely that the external vestibules of *Kv1.2*, *Kv1.3*, *IKCa1*, and *hSlo* are structurally similar to that of the *KcsA* channel.

To further evaluate the selectivity profile, we tested the most selective analog, ChTX-Glu^{32}, on a panel of four ChTX-resistant voltage-gated K^+ channels (*Kv1.1*, *Kv1.4*, *Kv1.5*, and *Kv3.1*) as well as on the apamin-sensitive, small-conductance Ca^{2+}-activated K^+ channel (SK_{Ca}) endogenously expressed in human Jurkat T-cells (27, 29). All five channels were resistant ($K_d \geq 5$ μM) to native ChTX as well as to ChTX-Glu^{32} (Fig. 7).

Concluding Remarks

In this study, we generated homology models of the pore regions of two prototypical mammalian K^+ channels, the voltage-gated *Kv1.3* channel and the Ca^{2+}-activated *IKCa1* channel, both present in human T-lymphocytes, based on their known structural similarity to the *KcsA* channel. Our *Kv1.3* model differs in detail from the previous models (4, 5), for example, in the orientation of the key residue Tyr^{400} in the selectivity filter. Guided by established ChTX-*Kv1.3* interactions, we docked this toxin in the *Kv1.3* model and used mutant cycle analysis to confirm the proximity of a pair of ChTX (Lys^{31}) and *Kv1.3* (Asp^{386}) residues predicted to be close. Since ChTX blocks *IKCa1* with roughly equivalent potency compared with *Kv1.3*, we hypothesized that ChTX might sit in the *IKCa1* vestibule with a similar geometry to that in *Kv1.3*. We therefore performed a docking simulation of ChTX in *IKCa1* for heuristic purposes. Multiple sets of predicted interactions were confirmed by mutant cycle analyses and then used to generate refined models of the docking configurations. Comparison of the two toxin-channel interfaces suggested a unique structural motif, a cluster of negatively charged residues present only in the Kv channel, that was exploited in the design and generation of three novel ChTX analogs. These analogs, containing negatively charged residues at toxin position 32, exhibit specificity for the *IKCa1* channel over *Kv1.3*. They do not block other voltage-gated and small-conductance Ca^{2+}-activated K^+ channels that lack this unique feature, but they inhibit *hSlo* channels, which resemble *IKCa1* in the turret region.

Our results strongly suggest that a polypeptide toxin with comparable affinities for different K^+ channels, even those belonging to widely divergent subfamilies (*e.g.* Ca^{2+}-activated *IKCa1* and voltage-gated *Kv1.3* channels), interacts with a topologically similar toxin-binding site in the external vestibule of these channels (Fig. 2). This has allowed us to start with a promiscuous polypeptide toxin (ChTX) that blocks multiple K^+ channels and to apply a comparative homology modeling approach to design novel analogs that selectively target intermediate- and large-conductance Ca^{2+}-activated K^+ channels. These ChTX analogs might be useful tools in elucidating the role of the *IKCa1* channel in cells that express ChTX-sensitive voltage-gated K^+ channels, but not *hSlo*, *e.g.* activated T-lymphocytes, erythrocytes, and colonic epithelia. Finally, our studies provide support for the feasibility of using the structure of the *KcsA* channel to guide the design of selective and potent inhibitors for a large variety of mammalian K^+ channels.

Acknowledgments—We appreciate the expert technical assistance of L. Forrest and A. C. Wu as well as valuable discussions with Drs. G. A. Gutman and C. M. Fanger. We thank Dr. C. Miller for the kind gift of the ChTX-Orn[27], ChTX-Gln[31], and ChTX-Glu[31] analogs and Dr. L. Toro for the kind gift of the *hSlo* construct.

REFERENCES

1. Stocker, M., and Miller, C. (1994) *Proc. Natl. Acad. Sci. U. S. A.* **91,** 9509–9513
2. Goldstein, S. A., Pheasant, D. J., and Miller, C. (1994) *Neuron* **12,** 1377–1388
3. Hidalgo, P., and MacKinnon, R. (1995) *Science* **268,** 307–310
4. Aiyar, J., Withka, J. M., Rizzi, J. P., Singleton, D. H., Andrews, G. C., Lin, W., Boyd, J., Hanson, D. C., Simon, M., Dethlefs, B., Lee, C., Hall, J. E., Gutman, G. A., and Chandy, K. G. (1995) *Neuron* **15,** 1169–1181
5. Aiyar, J., Rizzi, J. P., Gutman, G. A., and Chandy, K. G. (1996) *J. Biol. Chem.* **271,** 31013–31016
6. Ranganathan, R., Lewis, J. H., and MacKinnon, R. (1996) *Neuron* **16,** 131–139
7. Rauer, H., Pennington, M., Cahalan, M., and Chandy, K. G. (1999) *J. Biol. Chem.* **274,** 21885–21892
8. Doyle, D. A., Morais Cabral, J., Pfuetzner, R. A., Kuo, A., Gulbis, J. M., Cohen, S. L., Chait, B. T., and MacKinnon, R. (1998) *Science* **280,** 69–77
9. MacKinnon, R., Cohen, S. L., Kuo, A., Lee, A., and Chait, B. T. (1998) *Science* **280,** 106–109
10. Logsdon, N. J., Kang, J., Togo, J. A., Christian, E. P., and Aiyar, J. (1997) *J. Biol. Chem.* **272,** 32723–32726
11. Fanger, C. M., Ghanshani, S., Logsdon, N. J., Rauer, H., Kalman, K., Zhou, J., Beckingham, K., Chandy, K. G., Cahalan, M. D., and Aiyar, J. (1999) *J. Biol. Chem.* **274,** 5746–5754
12. Cahalan, M. D., and Chandy, K. G. (1997) *Curr. Opin. Biotechnol.* **8,** 749–756
13. Koo, G. C., Blake, J. T., Talento, A., Nguyen, M., Lin, S., Sirotina, A., Shah, K., Mulvany, K., Hora, D., Jr., Cunningham, P., Wunderler, D. L., McManus, O. B., Slaughter, R., Bugianesi, R., Felix, J., Garcia, M., Williamson, J., Kaczorowski, G., Sigal, N. H., Springer, M. S., and Feeney, W. (1997) *J. Immunol.* **158,** 5120–5128
14. Hanson, D. C., Nguyen, A., Mather, R. J., Rauer, H., Koch, K., Burgess, L. E., Rizzi, J. P., Donovan, C. B., Bruns, M. J., Canniff, P. C., Cunningham, A. C., Verdries, K. A., Mena, E., Kath, J. C., Gutman, G. A., Cahalan, M. D., Grissmer, S., and Chandy, K. G. (1999) *Br. J. Pharmacol.* **126,** 1707–1716
15. Khanna, R., Chang, M. C., Joiner, W. J., Kaczmarek, L. K., and Schlichter, L. C. (1999) *J. Biol. Chem.* **274,** 14838–14849
16. Brugnara, C. (1995) *Curr. Opin. Hematol.* **2,** 132–138
17. Brugnara, C., Armsby, C. C., Sakamoto, M., Rifai, N., Alper, S. L., and Platt, O. (1995) *J. Pharmacol. Exp. Ther.* **273,** 266–272
18. Brugnara, C., De Franceschi, L., Armsby, C. C., Saadane, N., Trudel, M., Beuzard, Y., Rittenhouse, A., Rifai, N., Platt, O., and Alper, S. L. (1995) *Ann. N. Y. Acad. Sci.* **763,** 262–271
19. Brugnara, C., Gee, B., Armsby, C. C., Kurth, S., Sakamoto, M., Rifai, N., Alper, S. L., and Platt, O. S. (1996) *J. Clin. Invest.* **97,** 1227–1234
20. Gardos, G. (1958) *Biochim. Biophys. Acta* **30,** 653–654
21. Ishii, T. M., Silvia, C., Hirschberg, B., Bond, C. T., Adelman, J. P., and Maylie, J. (1997) *Proc. Natl. Acad. Sci. U. S. A.* **94,** 11651–11656
22. Joiner, W. J., Wang, L. Y., Tang, M. D., and Kaczmarek, L. K. (1997) *Proc. Natl. Acad. Sci. U. S. A.* **94,** 11013–11018
23. Jensen, B. S., Strobaek, D., Christophersen, P., Jorgensen, T. D., Hansen, C., Silahtaroglu, A., Olesen, S. P., and Ahring, P. K. (1998) *Am. J. Physiol.* **275,** C848–C856
24. Vandorpe, D. H., Shmukler, B. E., Jiang, L., Lim, B., Maylie, J., Adelman, J. P., De Franceschi, L., Cappellini, M. D., Brugnara, C., and Alper, S. L. (1998) *J. Biol. Chem.* **273,** 21542–21553
25. Rufo, P. A., Merlin, D., Riegler, M., Ferguson-Maltzman, M. H., Dickinson, B. L., Brugnara, C., Alper, S. L., and Lencer, W. I. (1997) *J. Clin. Invest.* **100,** 3111–3120
26. Schreiber, G., and Fersht, A. R. (1995) *J. Mol. Biol.* **248,** 478–486
27. Grissmer, S., Nguyen, A. N., Aiyar, J., Hanson, D. C., Mather, R. J., Gutman, G. A., Karmilowicz, M. J., Auperin, D. D., and Chandy, K. G. (1994) *Mol. Pharmacol.* **45,** 1227–1234
28. Ho, S. N., Hunt, H. D., Horton, R. M., Pullen, J. K., and Pease, L. R. (1989) *Gene* (*Amst.*) **77,** 51–59
29. Grissmer, S., Lewis, R. S., and Cahalan, M. D. (1992) *J. Gen. Physiol.* **99,** 63–84
30. Grissmer, S., Nguyen, A. N., and Cahalan, M. D. (1993) *J. Gen. Physiol.* **102,** 601–630
31. Kalman, K., Pennington, M. W., Lanigan, M. D., Nguyen, A., Rauer, H., Mahnir, V., Paschetto, K., Kem, W. R., Grissmer, S., Gutman, G. A., Christian, E. P., Cahalan, M. D., Norton, R. S., and Chandy, K. G. (1998) *J. Biol. Chem.* **273,** 32697–32707
32. Rauer, H., and Grissmer, S. (1996) *Mol. Pharmacol.* **50,** 1625–1634
33. Rauer, H., and Grissmer, S. (1999) *Br. J. Pharmacol.* **127,** 1065–1074
34. Dauplais, M., Lecoq, A., Song, J., Cotton, J., Jamin, N., Gilquin, B., Roumestand, C., Vita, C., de Medeiros, C. L. C., Rowan, E. G., Harvey, A. L., and Menez, A. (1997) *J. Biol. Chem.* **272,** 4302–4309
35. Tudor, J. E., Pallaghy, P. K., Pennington, M. W., and Norton, R. S. (1996) *Nat. Struct. Biol.* **3,** 317–320
36. Grupe, A., Schroter, K. H., Ruppersberg, J. P., Stocker, M., Drewes, T., Beckh, S., and Pongs, O. (1990) *EMBO J.* **9,** 1749–1756
37. Munujos, P., Knaus, H. G., Kaczorowski, G. J., and Garcia, M. L. (1995) *Biochemistry* **34,** 10771–10776
38. Garcia, M. L., Knaus, H. G., Munujos, P., Slaughter, R. S., and Kaczorowski, G. J. (1995) *Am. J. Physiol.* **269,** C1–C10
39. Kirsch, G. E., Drewe, J. A., Verma, S., Brown, A. M., and Joho, R. H. (1991) *FEBS Lett.* **278,** 55–60